International Conference on Space Optics—ICSO 2024

Antibes Juan-les-Pins, France 21-25 October 2024

Edited by Philippe Kubik, Frédéric Bernard, Kyriaki Minoglou and Nikos Karafolas

Camera Calibration with Diffractive Optical Elements for the PLATO Mission





Camera Calibration with Diffractive Optical Elements for the PLATO Mission

Denis Grießbach¹, Francesca Molendini², Manuel Adler Abreu³, Nuno M. Gonçalves³, and Martin Pertenais¹

¹German Aerospace Center (DLR), Institute of Optical Sensor Systems, Rutherfordstr. 2, 12489 Berlin, Germany

 ²European Space Agency, Keplerlaan 1, 2201AZ, Noordwijk, NL
 ³Faculty of Sciences - University of Lisbon, Institute of Astrophysics and Space Sciences, Laboratory of Optics Lasers and Systems, Campo Grande, Lisboa, Portugal

ABSTRACT

PLATO – PLAnetary Transits and Oscillation of stars – is a medium-class mission in the European Space Agency (ESA) Cosmic Vision programme, whose launch is foreseen by 2026. The objective is the detection and characterization of terrestrial exoplanets up to the habitable zone of solar-type stars by means of their transit signature in front of a very large sample of bright stars. The PLATO payload consists of an instrument with 26 cameras for star observation; 24 normal cameras grouped in four subsets with six cameras each and two fast cameras. Besides providing scientific data for very bright stars, the fast cameras also serve as two redundant Fine Guidance Systems (FGSs) and will be an integral part of the Attitude and Orbit Control System (AOCS).

To ensure the best possible performance, all cameras are pre-calibrated on ground, including a best focus determination as well as a geometric calibration. Traditionally, this is done with a gimbal/hexapod setup to illuminate different parts of the Field of View (FoV) with a collimated light source. This method is tedious, time-consuming, and limited in the achievable precision. Therefore, a backup solution using a Diffractive Optical Element (DOE) is proposed. The DOE acts as a beam splitter and provides a precise holographic pattern with well-known diffraction angles. Instead of combining images from different FoV positions, a single exposure is sufficient to geometrically calibrate a camera. Furthermore, this method is used to determine the best focus of the camera.

Keywords: PLATO, Camera calibration, Diffractive Optical Element, DOE

1. INTRODUCTION

Many scientific space missions, including PLATO,¹ consists of an optical payload which needs to be characterized and calibrated in terms of radiometry and geometry. This work is primarily concerned with the geometric calibration and the focus determination of the Engineering Model (EM) camera for PLATO. It is part of an extensive on-ground test campaign to verify the integration of each camera and provide an initial characterization. This step is especially important for the two fast cameras which also serve as Fine Guidance Systems (FGSs).²

The geometric camera calibration is routinely done with a gimbal/hexapod setup which illuminates different parts of the FoV with a collimated light source. This method is tedious, time-consuming, and limited in the level of precision achievable. It can be replaced with a Diffractive Optical Element (DOE) which works as a beam splitter and provides a precise holographic pattern with well-known diffraction angles. Thus, a single exposure is sufficient to geometrically calibrate a camera.³ Therefore, the setup is drastically simplified as the instrument does not have to be rotated. This is especially useful considering the high demands for a mechanical setup placed in a Thermal Vacuum (TV) chamber. Furthermore, this method can be used to determine the best focus of the camera.

 $Further\ author\ information:\ Send\ correspondence\ to\ denis.griessbach@dlr.de$

2. DIFFRACTIVE OPTICAL ELEMENTS

DOEs can be used to split an incoming collimated beam with wavelength λ into a number of beams with well-known propagation directions. As the image on the sensor is a Fraunhofer diffraction pattern, each projected image point represents a point at infinity, denoted by the direction vector

$$\mathbf{d} = \begin{pmatrix} \lambda \nu_x, & \lambda \nu_y, & \sqrt{1 - \lambda^2 (\nu_x^2 + \nu_y^2)} \end{pmatrix}^T, \tag{1}$$

where $\nu_{x,y} = n_{x,y}/g_{x,y}$ are the spatial frequencies encoded in the DOE, with grating constants (g_x, g_y) and (n_x, n_y) denoting the particular diffraction orders. The grating vectors define the DOE-Reference Frame (RF). With suitable computational algorithms⁴ it is possible to encode spatially aperiodic DOEs with arbitrary spatial frequencies, choosing the propagation directions freely. As they are easier to design for the large aperture diameters needed, spatially periodic DOEs were used here.

Note, however, that equation 1 is only valid if the incident light is a plane wave with uniform intensity distribution, perfectly perpendicular to the DOE-RF. In a real setup, the beam is finite in extension and often has a non-uniform intensity profile, which is typically Gaussian. Moreover, a slight tilt of the DOE with respect to the incident beam is hard to avoid.

The deviations of the real beam profile from a plane wave cause the diffraction spots in the far field to have a certain size, which can be estimated from the convolution theorem of Fourier optics.⁵ For a more detailed analysis, a laser beam can be expressed by its angular spectrum. The consequent propagation directions are determined with the diffraction formula for non-perpendicular incidence to the DOE, which needs to be applied in our analysis anyway because of the potentially unavoidable tilt of the DOE with respect to the incident laser beam. For the following analysis, the DOE-RF will be used, in which the incident beam is given by

$$r = (\sin(\beta), -\sin(\alpha)\cos(\beta), \cos(\alpha)\cos(\beta))^T,$$
 (2)

with the angles α and β rotating the x- and y-axes of the DOE-RF w.r.t. the collimated beam. The directions of the diffracted beams are now obtained as follows⁶

$$\mathbf{d} = (\lambda \nu_x + r_x, \quad \lambda \nu_y + r_y, \quad \sqrt{1 - (\lambda \nu_x + r_x)^2 - (\lambda \nu_y + r_y)^2})^T. \tag{3}$$

3. CAMERA MODEL

To map the direction vector d, given in the DOE-RF, it first needs to be transformed to the camera Boresight (BS)-RF⁷ with

$$\begin{pmatrix} X \\ Y \\ Z \end{pmatrix}^{BS} = \mathbf{R}_{DOE}^{BS} \mathbf{d}, \tag{4}$$

where $\mathbf{R}_{DOE}^{BS}(\omega, \varphi, \kappa)$ is the exterior orientation of the camera BS-RF w.r.t the DOE-RF. Considering projective geometry, the normalized camera coordinate $(x, y)^T$ can be recovered by dividing the homogeneous coordinate $(xZ, yZ, Z)^T$ by its non-zero factor -Z. This can be seen as a projection to a virtual plane at Z = -1, being the normalized Focal Plane Assembly (FPA) plane.

3.1 Interior Orientation

As shown in fig. 1, a special feature of the PLATO cameras is the four CCD setup. For each individual CCD-RF an additional transformation $R_{BS}^{CCD} = R_z(\gamma)R_y(\pi)$ is needed. This includes $R_z(\gamma)$ allowing for the 90° rotations of the CCDs about the optical axis and $R_y(\pi)$ being a 180° rotation about the y-axis. The latter is needed to align the anti-parallel virtual z-axis of the CCD-RFs to the BS-RF z-axis, also known as the optical axis. By

definition the optical axis is perpendicular to the FPA. The pixel coordinate $(u, v)^T$, given in the CCD-RF is now determined from the boresight coordinates with

$$\begin{pmatrix} u \\ v \\ 1 \end{pmatrix} = KR_{BS}^{CCD} \begin{pmatrix} x \\ y \\ -1 \end{pmatrix}^{BS}, \tag{6}$$

where the camera matrix K represents a pinhole camera model, containing the principle point $(u_0, v_0)^T$ and the effective focal length f, which in this context is the distance of the perspective centre (pinhole) to the FPA. The principal point, as used here, is the point where the optical axis intersects with the FPA. It is given w.r.t. the origin of the individual CCD-RF.

$$\mathbf{K} = \begin{bmatrix} f & 0 & u_0 \\ 0 & f & v_0 \\ 0 & 0 & 1 \end{bmatrix} \tag{7}$$

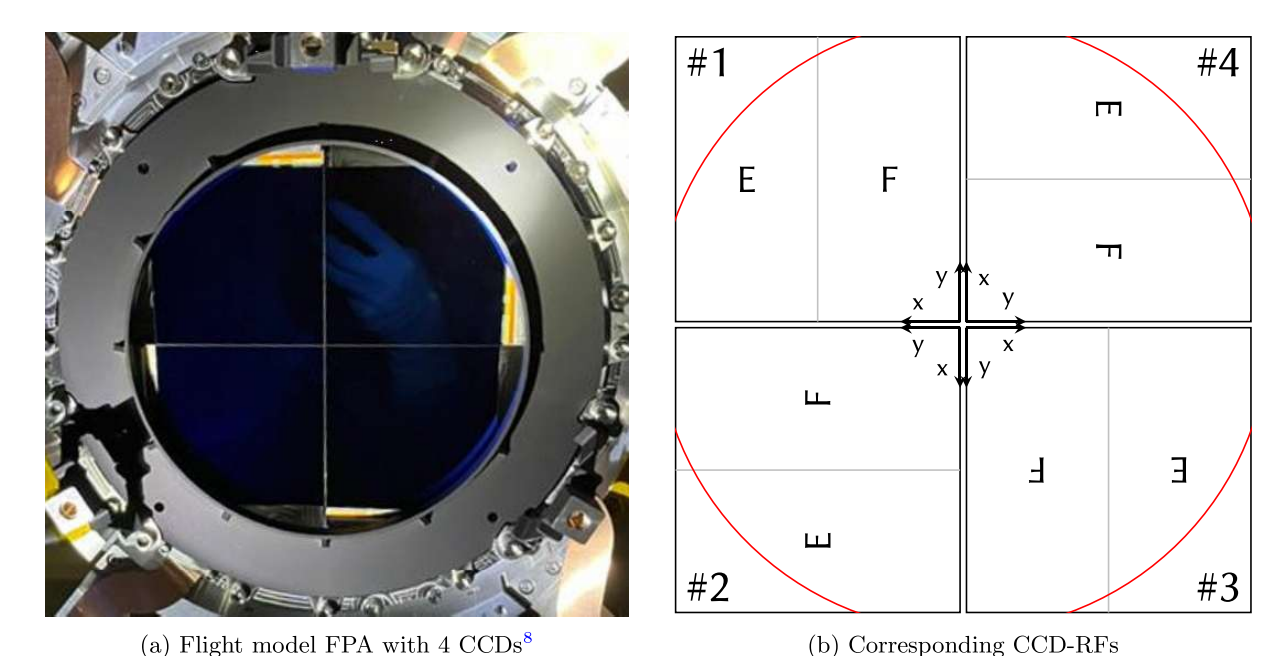


Figure 1: Normal camera configuration

3.2 Distortion Model

Since the pinhole model does not consider lens distortion, it is extended by the Brown-Conrady model. It consists of a radial-symmetric component δ_r , describing pincushion/barrel distortion, and a tangential component δ_t . Normalized boresight coordinates are corrected as follows.

$$\begin{pmatrix} x_d \\ y_d \end{pmatrix} = \begin{pmatrix} x \\ y \end{pmatrix} + \boldsymbol{\delta}_r(x, y, \boldsymbol{k}) + \boldsymbol{\delta}_t(x, y, \boldsymbol{p})$$
 (8)

The radial-symmetric model with the radial distance $r^2 = x^2 + y^2$ is expressed as

$$\boldsymbol{\delta}_r(x, y, \boldsymbol{k}) = \begin{pmatrix} x \\ y \end{pmatrix} (k_1 r^2 + k_2 r^4 + k_3 r^6 + \cdots). \tag{9}$$

Although there is no tangential distortion with a nominal lens design, it occurs due to manufacturing and alignment tolerances, e.g. decentered, shifted lenses. First introduced by Conrady and adopted by Brown,⁹ tangential distortion, also known as decentering distortion, is modelled with

$$\boldsymbol{\delta}_t(x,y,\boldsymbol{p}) = \begin{pmatrix} p_1(3x^2 + y^2) + 2p_2xy \\ p_2(x^2 + 3y^2) + 2p_1xy \end{pmatrix} (1 + p_3r^2 + p_4r^4 \cdots).$$
(10)

3.3 Calibration Methodology

The parameters of the camera model are found by means of a non-linear optimization, using measured and therefore distorted image coordinates and their corresponding target directions. A calibration pattern is usually realized by rotating the instrument in front of a collimated beam which illuminates its whole aperture. Dependent on the incident angle, the beam is focused on a single CCD position, referred to as measurement. With a DOE as a beam splitter, it is possible to measure all diffracted beam directions with one exposure.

3.3.1 Centroid Estimation

Before starting the model optimization, the measured image coordinates need to be extracted. First, the images are pre-processed by subtracting the read-out smearing recorded in the over-scan rows as shown in fig. 2a. To estimate the position of each mapped diffraction order, it's Point Spread Function (PSF) is approximated as an ideal Gaussian. The integrated flux over one pixel is modelled as

$$\boldsymbol{h}(i,j) = I_m \cdot \frac{1}{2\pi\sigma^2} \int_{i-0.5}^{i+0.5} e^{-\frac{(u-u_c)^2}{2\sigma^2}} du \int_{j-0.5}^{j+0.5} e^{-\frac{(v-v_c)^2}{2\sigma^2}} dv + D + \xi,$$
(11)

with the centroid position (u_c, v_c) , PSF width σ , intensity I_m , background D, and random noise ξ . With an ideal laser source this model would be sufficient to estimate the PSF parameters by means of a non-linear least-square optimization.

However, following eq. (1) it can be seen that the bandwidth of the used wavelength λ will lead to an uncertainty in the produced target direction. Consequently, the mapped image point will be smeared as seen in fig. 2. By using eqs. (5) and (6) and ignoring second order effects like lens distortion and DOE tilt, the smearing can be quantified with

$$\sigma_{uv} = \frac{\partial uv}{\partial \lambda} \sigma_{\lambda} = f \frac{\frac{\partial \mathbf{d}_{xy}}{\partial \lambda} \mathbf{d}_z - \mathbf{d}_{xy} \frac{\partial \mathbf{d}_z}{\partial \lambda}}{\mathbf{d}_z^2} \sigma_{\lambda}, \tag{12}$$

where σ_{λ} is the bandwidth of the light source, shown in table 1. with the given camera focal length, the smearing effect is as big as ± 10 pixel on the FoV edges. Combining eq. (11) and eq. (12), the observed PSF can be seen as the convolution of an ideal 2d-Gaussian with a smearing kernel.

$$y = h * s \tag{13}$$

The smearing kernel s is constructed as a 1d-Gaussian using σ_{uv} , the current best estimate of (u_c, v_c) , and a rotation towards the zero diffraction order. Including the kernel in the least-square optimization also allows to estimate the bandwidth of the laser source.

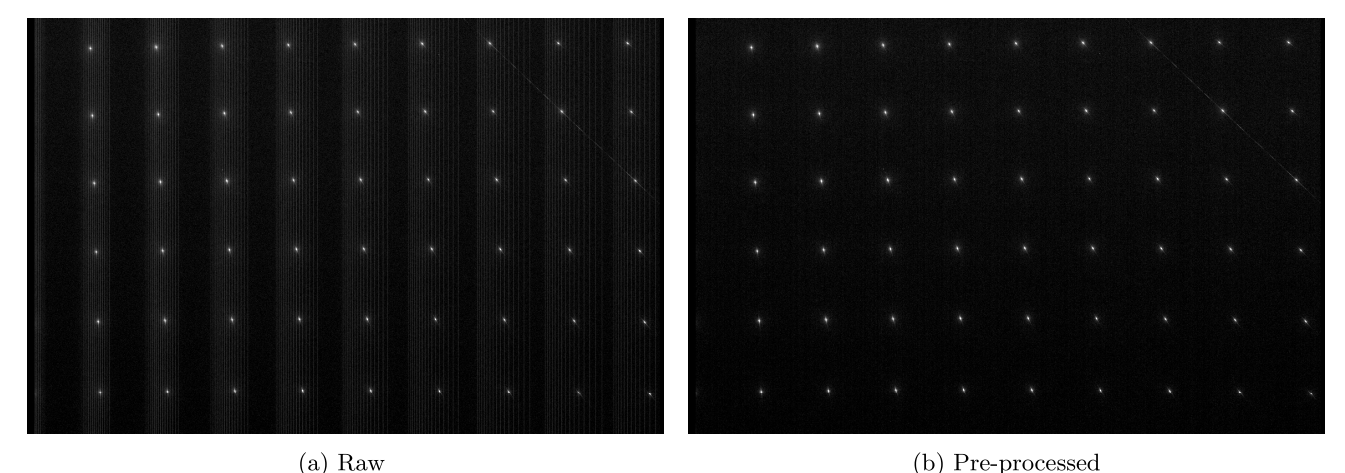


Figure 2: Measured red calibration pattern with scaled dynamic range, 1500 rows of CCD 4F

3.3.2 Camera Model Estimation

Using eq. (6), distorted image coordinates (u_d, v_d) are given with

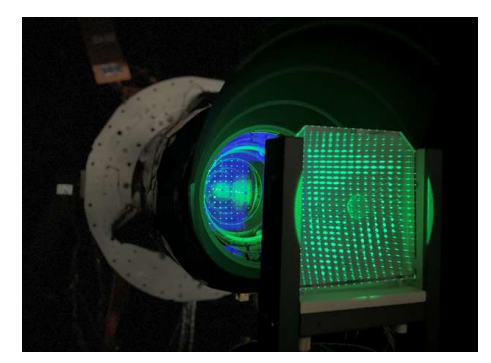
$$\begin{pmatrix} u_d \\ v_d \\ 1 \end{pmatrix} = KR_{BS}^{CCD} \begin{pmatrix} x_d \\ y_d \\ -1 \end{pmatrix}. \tag{14}$$

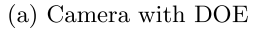
Applying eqs. (4) to (6) and (8), the distorted normalized camera coordinates (x_d, y_d) are calculated from their model directions, which are transformed to the camera BS-RF, projected to a virtual plane at distance z = -1, distorted according to the distortion model, and brought to the CCD-RF. To estimate the camera model we seek to minimize the errors in distorted image space using the cost function

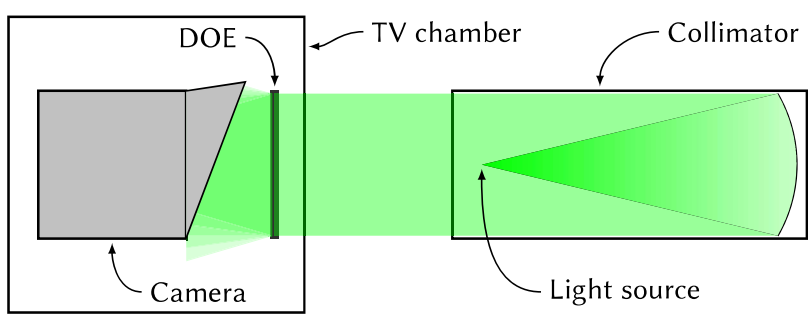
$$\min_{m} \left\| \begin{pmatrix} \hat{u}_d \\ \hat{v}_d \end{pmatrix} - \begin{pmatrix} u_d \\ v_d \end{pmatrix} \right\|^2, \tag{15}$$

with (\hat{u}_d, \hat{v}_d) , the measured distorted image coordinates and $m = (f, u_0, v_0, \mathbf{k}, \mathbf{p}, \omega, \varphi, \kappa, \alpha, \beta)^T$, being the focal length, the principle point position, and the distortion parameters. Note that the exterior orientation of the BS-RF w.r.t. the DOE-RF $(\omega, \varphi, \kappa)$ as well as the DOE tilt angles (α, β) are usually unknown and therefore need to be part of the optimization.

4. EXPERIMENTAL SETUP







(b) Schematic setup

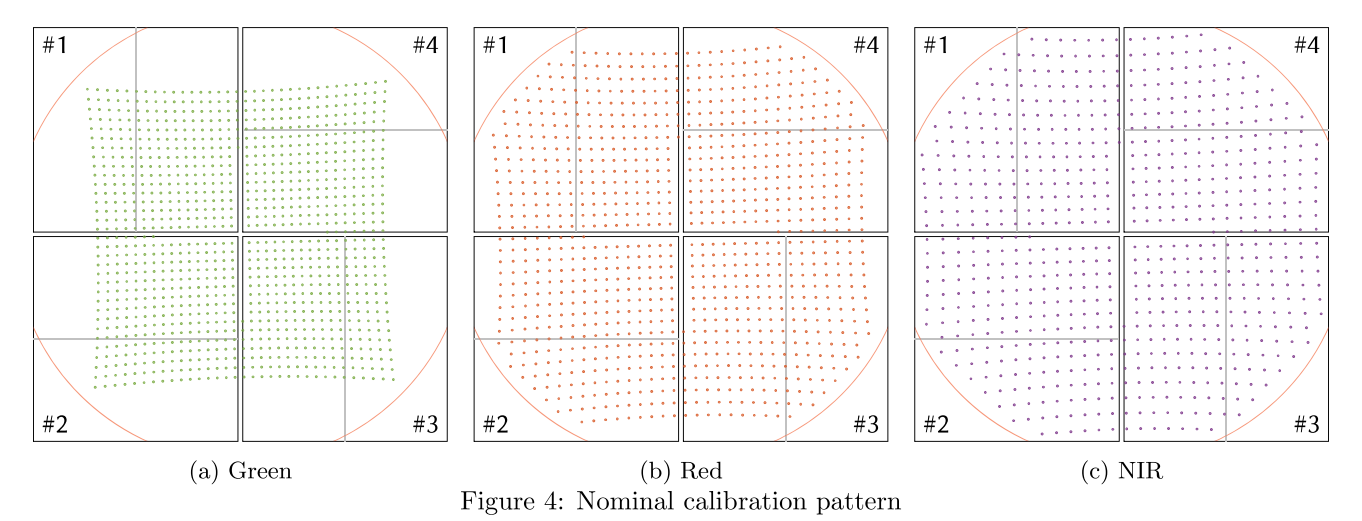
Figure 3: Experimental setup

To calibrate a camera as part of a space instrument, it is mandatory to operate it in the right environmental conditions. Therefore, the setup needs to be partly placed in a Thermal Vacuum (TV) chamber, providing vacuum and a nominal temperature of $-80\,^{\circ}$ C. It features an optical window to couple collimated light into the chamber. A room temperature collimator, ¹⁰ based on an on-axis parabolic mirror, collimates light from an optical fibre. This allows to couple different light sources with wavelength as shown in table 1. Since the diffraction angles are wavelength dependent, the DOE does not support a white light calibration. However, by calibrating with green, red and Near Infrared (NIR) illumination, a white light equivalent can be calculated according to the spectral sensitivity of the camera. The used Fabry-Pérot laser diodes allow for a cost-effective setup but feature a larger bandwidth compared to standard laser sources.

Table 1: Diode laser sources¹⁰

	Green	Red	NIR
Wavelength [nm] Bandwidth (FWHM) [nm]	517.9 2.0	642.8 1.5	782.8 2

As shown in eq. (1), the encoded spatial frequencies determine the properties of the DOE. With a grating constant of 37.6 μ m and ± 16 diffraction orders, 33×33 potential target directions can be produced, covering the $\pm 18.9^{\circ}$ FoV of the PLATO cameras. The PLATO CCDs are read without a shutter. To avoid contamination of multiple measurements in the same column by the resulting readout smearing, shown in fig. 2a, the DOE has been mounted with a 1.5° rotational offset around the optical axis, as seen in fig. 4.



5. RESULTS

In order to prove the feasibility of the proposed approach, the EM camera for the PLATO mission has been calibrated at the European Space Agency (ESA) test facility by using a fixed setup with the DOE in flight environment representative conditions. Earlier round-robin tests with the same camera at the Netherlands Institute for Space Research (SRON), Institut d'Astrophysique Spatiale (IAS), and Instituto Nacional de Técnica Aeroespacial (INTA) have been using a traditional gimbal/hexapod setup to rotate the camera in front of a collimated white light source.¹¹ Despite the fundamentally different approaches, the results are expected to lie within the margins of error.

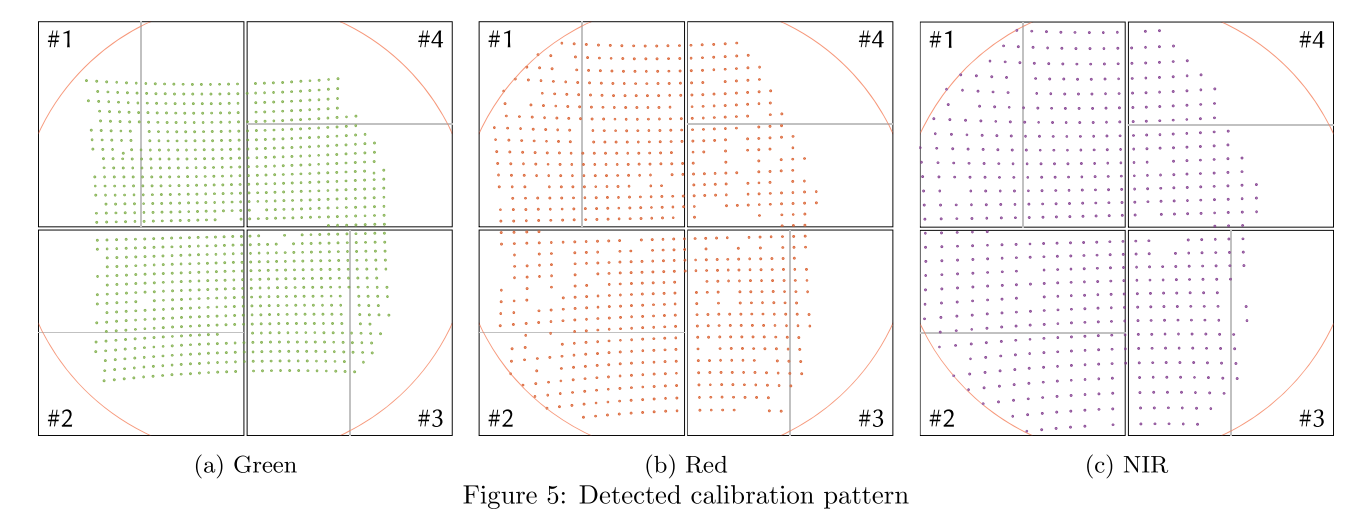


Figure 5 shows the measured calibration pattern for all three wavelengths. Due to a slight misalignment of the collimated beam, in combination with the mechanical vignetting of the beam, only 70–85% of all possible targets have been detected. The mechanical vignetting also leads to an uneven intensity distribution throughout the FoV, influencing the Signal to Noise Ratio (SNR) of the detected points. Nonetheless, compared to the 40

FoV positions obtained with the traditional method, this is still superior and does not pose a problem for the calibration. After extracting the centroid information from the images according to section 3.3.1, the camera model is estimated following section 3.3.2.

5.1 Best Focus Temperature

The PLATO cameras are equipped with a thermal re-focus mechanism which allows to focus the camera. To find the Best Focus Temperature (BFT), the EM camera has been tested at different temperature plateaus from -70 to -90 °C in 5 °C steps. Nominally, the best focus of all PLATO cameras is determined by means of the en-squared energy, which is a measure of the PSF size. 12

Besides the geometric calibration shown in section 5.2, the calibration pattern produced by the DOE can also be used to quantify the focus of the camera.¹³ As discussed in section 3.3.1, the PSF width σ is estimated for each centroid. This allows to use the average PSF size of all spots as an alternative measure of the camera focus. Figure 6 shows 3th-order polynomials fitted to the average PSF size of each plateau for each test house. The calculated BFT for the DOE measurement lies within the variation of all test houses. This variation is attributed to the environmental conditions in the different TV chambers which can not guarantee the same temperature distribution within the camera.

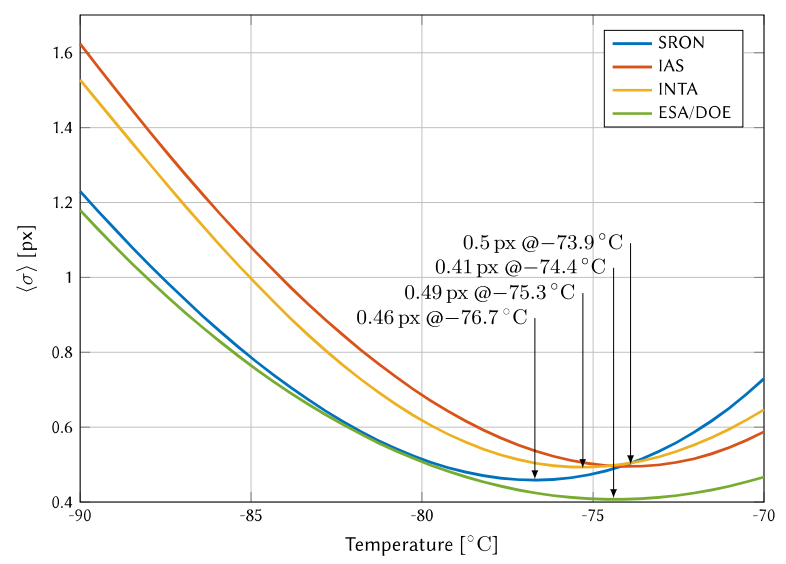


Figure 6: Best focus temperature comparison

5.2 Geometric Calibration

Table 2 shows the camera parameters for each test house at its individual BFT. As a white light illumination is not feasible for the DOE, a white light equivalent has been calculated as the weighted mean of the three used wavelength. The weights are given with 0.75, 0.85 and 0.65 for green, red and NIR respectively, being the spectral sensitivity of the camera. Compared to the other test houses, the distortion parameters as well as the mechanical parameters, e.g. CCD positions agree well and lie within the margin of error. The focal length varies by up to 2%, which can be ascribed to the different light sources and collimators used.

The residual error p95 is calculated from eq. (15) and gives the 95 percentile of the resulting absolute error. Whereas the residual error for the conventional approach is dominated by the mechanical accuracy of the rotation stages, this cannot be the case for the DOE measurement. Here, additional noise is caused by non-ideal illumination with low SNR in some regions. A possible mitigation would be to decrease the distance between DOE and camera which would improve the mechanical vignetting and lead to a more even intensity distribution. As the CCDs can only be read sequentially, without the option to reduce the camera integration time, mechanical vibrations of the TV chamber are suspected to increase the noise across CCDs.

		DOE @ ESA			SRON	IAS	INTA	
		green	red	NIR	white eq.	white	white	white
	f	13 736.059	13 727.314	13 729.579	13 730.883	13 746.860	13 758.320	13 746.862
	k_1	0.316	0.321	0.323	0.320	0.320	0.321	0.324
	k_2	0.181	0.087	0.065	0.112	0.075	0.086	0.034
	k_3	0	0	0	0	0	0	0
	u_0	-45.02	-38.64	-40.85	-41.40	-45.98	-42.2	-36.27
CCD #1	v_0	-10.80	-7.49	-8.02	-8.75	-7.38	-8.73	-14.39
	$\Delta \gamma$	0	0	0	0	0	0	0
	u_0	-59.22	-62.39	-62.34	-61.32	-61.07	-60.37	-55.54
CCD $\#2$	v_0	-8.46	-2.35	-4.13	-4.90	-11.09	-6.70	-0.04
	$\Delta \gamma$	-2.42	-23.96	-42.97	-22.27	8.87	-31.90	-110.62
	u_0	-62.10	-68.49	-66.40	-65.76	-58.70	-62.77	-69.24
CCD $\#3$	v_0	-22.81	-25.88	-25.77	-24.83	-25.80	-24.66	-19.58
	$\Delta \gamma$	-6.07	-28.10	-23.63	-19.47	-23.60	7.82	38.92
	u_0	-47.89	-44.70	-45.20	-45.91	-43.75	-44.88	-50.30
CCD $\#4$	v_0	-25.03	-31.53	-29.32	-28.73	-22.45	-26.91	-32.57
	$\Delta \gamma$	-27.35	-24.25	-21.59	-24.52	-45.44	12.77	172.30
	p95	0.49	0.38	0.41	0.43	0.57	0.33	1.33

Table 2: Calibration parameters* @ BFT *f , u_0 , v_0 , p95 in [px]. $\Delta \gamma$ in [arcsec]

6. CONCLUSION

This paper provides a proof of concept of an alternative method to calibrate a camera as part of a space instrument. Here, the Engineering Model (EM) camera of the PLATO Payload has been used to determine the geometric camera calibration parameters as well as the Best Focus Temperature (BFT).

The achieved results are highly consistent with the calibrations obtained independently at three different test houses using the conventional gimbal/hexapod approach. By using a DOE the camera does not need to rotate in front of the collimated beam. This reduces the complexity of the experimental setup noticeably. It also increases the precision of the calibration as it eliminates systematic errors introduces by the Mechanical Ground Support Equipment (MGSE). At the same time, it speeds up the procedure because only one exposure of the calibration pattern already contains all the needed information. Furthermore, the density of the calibration pattern has been drastically increased, which in turn decreases the uncertainty of the estimated camera parameters. By changing the DOE specification, the number of calibration targets can be easily scaled to meet requirements.

Since the DOE calibration pattern is wavelength dependent, a white light illumination is not directly feasible. Therefore, a white light equivalent has been calculated from three calibrations with green, red, and NIR light sources. This could also provide an opportunity for characterization of the chromatic aberration of the camera.

The main shortcoming of this first measurement campaign is the rather uneven intensity distribution due to mechanical vignetting and a slight misalignment of the collimated beam with respect to the camera aperture. Both problems can be mitigated by mechanical adjustments to the setup. Also, the choice of the laser sources itself, dictated by limited budget and procurement time, was necessarily not optimal as the increased bandwidth led to smearing of the point sources, increasing the complexity of the PSF estimation and decreases the measurement accuracy. This can be improved by using gas laser sources with a much smaller bandwidth. Nonetheless, the use of a DOE shows great potential to be a superior method for camera calibration compared to the conventional approach.

Acknowledgments

This work presents results from the European Space Agency (ESA) space mission PLATO. The PLATO payload, the PLATO Ground Segment and PLATO data processing are joint developments of ESA and the PLATO Mission Consortium (PMC). Funding for the PMC is provided at national levels, in particular by countries participating in the PLATO Multilateral Agreement (Austria, Belgium, Czech Republic, Denmark, France, Germany, Italy, Netherlands, Portugal, Spain, Sweden, Switzerland, Norway, and United Kingdom) and institutions from Brazil. A special thanks for the whole ESA team which made this campaign possible. Members of the PLATO Consortium can be found at https://platomission.com/. The ESA PLATO mission website is https://www.cosmos.esa.int/plato.

REFERENCES

- [1] J. L. Alvarez, T. Walloschek, A. Heras, et al., "The planetary transit and oscillations (PLATO) mission status: flight model build and initial ground testing," in *Space Telescopes and Instrumentation 2024: Optical, Infrared, and Millimeter Wave*, L. E. Coyle, S. Matsuura, and M. D. Perrin, Eds., **13092**, 1309215, International Society for Optics and Photonics, SPIE (2024).
- [2] D. Grießbach, U. Witteck, and C. Paproth, "The fine guidance system of the PLATO mission," in *International Conference on Space Optics ICSO 2020*, B. Cugny, Z. Sodnik, and N. Karafolas, Eds., **118523**H, International Society for Optics and Photonics, SPIE (2021).
- [3] D. Grießbach, M. Bauer, A. Hermerschmidt, et al., "Geometrical camera calibration with diffractive optical elements," Optics Express 16(25), 20241–20248 (2008).
- [4] A. Hermerschmidt, S. Krüger, and G. Wernicke, "Binary diffractive beam splitters with arbitrary diffraction angles," *Opt. Lett.* **32**, 448–450 (2007).
- [5] J. W. Goodman, Introduction to Fourier Optics, Roberts & Company Publishers, 3rd ed. (2005).
- [6] R. C. McPhedran, G. H. Derrick, and L. Brown, "Theory of crossed gratings," in *Electromagnetic theory of gratings*, R. Petit, Ed., 227–275, Springer Verlag Berlin (1980).
- [7] European Cooperation for Space Standardization, Stars sensors terminology and performance specification, no. ECSS-E-ST-60-20C, ESA Publications Division (2008).
- [8] "PLATO Normal FPA FM12 Outgoing Inspection Report," Tech. Rep. PLATO-INT-PL-RP-0171 (2023-12-14).
- [9] D. C. Brown, "Close-range camera calibration," Photogrammetric Engineering 37(8), 855–866 (1971).
- [10] M. Abreu, A. Cabral, and N. Gonçalves, "Room temperature collimator performance and calibration report collimator unit #3," tech. rep., University of Lisbon, Laboratory of Optics Lasers and Systems Institute of Astrophysics and Space Sciences (12-09-2023).
- [11] F. Borsa, A. Cottinelli, N. Gorius, et al., "PLATO EM first cryogenic vacuum test campaign PSF results," in Space Telescopes and Instrumentation 2022: Optical, Infrared, and Millimeter Wave, L. E. Coyle, S. Matsuura, and M. D. Perrin, Eds., 12180, 121801D, International Society for Optics and Photonics, SPIE (2022).
- [12] M. Pertenais, J. Cabrera, D. Griessbach, et al., "Overview of PLATO's cameras on-ground and in-orbit calibration and characterisation," in *International Conference on Space Optics — ICSO 2020*, B. Cugny, Z. Sodnik, and N. Karafolas, Eds., 11852, 1185209, International Society for Optics and Photonics, SPIE (2021).
- [13] M. Pertenais, C. Ryan, S. Rodd-Routley, et al., "Usage of a Diffractive Optical Element (DOE) for best focal plane estimation of a camera during the integration process," in Advances in Optical and Mechanical Technologies for Telescopes and Instrumentation V, R. Navarro and R. Geyl, Eds., 12188, 121883Z, International Society for Optics and Photonics, SPIE (2022).